SCIENTIFIC REPORTS

Phase Transformation Evolution in NiTi Shape Memory Alloy under Cyclic Nanoindentation Loadings at Dissimilar Rates

Abbas Amini[1,2], Chun Cheng[3], Qianhua Kan[4], Minoo Naebe[5] & Haisheng Song[6]

[1]Department of Chemical and Biomolecular Engineering, The University of Melbourne, Parkville, VIC 3010, Australia, [2]frontierTECH, Melbourne, VIC 3141, Australia, [3]Department of Materials Science and Engineering, South University of Science and Technology of China, Shenzhen, Guangdong 518055, P. R. China, [4]School of Mechanics and Engineering, Southwest Jiaotong University, Chengdu, Sichuan 610031, P. R. China, [5]Institute for Frontier Materials (IFM), Deakin University, Waurn Ponds, VIC 3217, Australia, [6]Wuhan National Laboratory for Optoelectronics (WNLO) and the School of Optical and Electronic Information, Huazhong University of Science and Technology, Wuhan 430074, P. R. China.

Hysteresis energy decreased significantly as nanocrystalline NiTi shape memory alloy was under triangular cyclic nanoindentation loadings at high rate. Jagged curves evidenced discrete stress relaxations. With a large recovery state of maximum deformation in each cycle, this behavior concluded in several nucleation sites of phase transformation in stressed bulk. Additionally, the higher initial propagation velocity of interface and thermal activation volume, and higher levels of phase transition stress in subsequent cycles explained the monotonic decreasing trend of dissipated energy. In contrast, the dissipated energy showed an opposite increasing trend during triangular cyclic loadings at a low rate and 60 sec holding time after each unloading stage. Due to the isothermal loading rate and the holding time, a major part of the released latent heat was transferred during the cyclic loading resulting in an unchanged phase transition stress. This fact with the reorientation phenomenon explained the monotonic increasing trend of hysteresis energy.

T hermomechanical NiTi shape memory alloys (SMAs) have been used extensively for intricate processes in high tech industries due to their excellent self-controlled and simple mechanisms[1]. The range of applications for these smart materials has covered bio-, nano- and macro- technologies, e.g., coils to treat damaged vascular systems, artificial heart tissues, blood clot removers, porous structures for artificial joints, nano-dampers and composites for aircraft elements[2]. In all these applications, NiTi SMA is under cyclic loadings with different setups, magnitudes and rates[3]. NiTi SMA accommodates a large amount of inelastic deformation by atomic lattice rearrangements called discrete forward and reverse phase transformation[4]. In this transition, the parent austenite phase (B2) and a shear-like distorted-monoclinic martensite phase (B19′) revert to each other with release or absorption of latent heat. A shape recovery is obtained after removal of the load (superelasticity) or upon an application of heat (shape memory effect). This implies that the governing parameters for a thermoelastic NiTi SMA is stress, temperature and their thermal-mechanical loading histories, e.g., rates, cycles, and loading set ups[5–11]. These parameters have been thoroughly studied in uniaxial macro-scale torsional, bending and especially tensile conditions[12–19]. Recently, developed technologies, i.e., in-situ nanoindentation machines, have provided a great capability to reveal the behavior of NiTi SMAs[20–26] and other materials[27–30] under nano-scale and atomistic level compression.

In cyclic-compressive loadings, the temperature and initial stress of each cycle and their correlation are key parameters because a slight change in these parameters results in a huge change in the martensite volume in subsequent cycles[12,14,31–33]. Thus, due to a significant influence on the alloy's behaviour, the thermal effect cannot be neglected in the case of a dynamic/cyclic loading[34]. In addition, recent studies have shown a different nature of heat transfer phenomenon in extremely small scale compared to a macro scale[35]. A different paradigm of heat transfer was also presented during ultrafast loadings. Nevertheless, these recent advances have been overlooked within literature and need to be accounted for predicting the nanoscale behavior of thermomechanical smart materials[8,9,27]. In this paper, it is theoretically and experimentally demonstrated that the thermal effect, the activation volume, the orientation and the velocity of interface propagation determine the performance of

NiTi SMA under cyclic nanoindentation loadings. A concomitant hypothesis is provided for the wake of phase transformation volume in a nanoscale bulk according to the trend of nanoindentation curves. A numerical simulation is also provided with its constitutive assumptions to support the results.
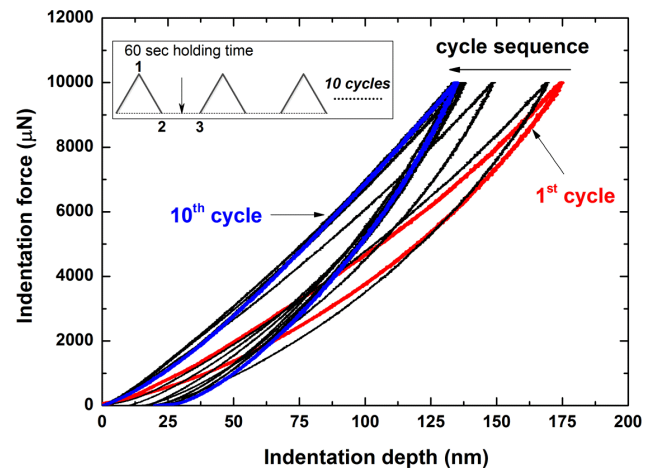
Results

Fig. 1 shows the jagged indentation curves of the cyclic loading on NiTi SMA with a triangular set up (inset Fig. 1). With no holding time, a consecutive load was instantly applied on the sample after a loading-unloading cycle was completed. In each cycle, the load started from zero to a maximum 10000 µN, which was constant for all cycles. The loading and unloading rates were similar, 2×10^3 µNsec^{-1}. Each cycle had a low plastic deformation, however, an accumulated deformation still existed at the end. A slight increase in the maximum indentation depth during the 10-cyclic loading was observed. The maximum hysteresis area was witnessed in the first cycle, while the last cycle indicated the lowest dissipation energy. Similar results were obtained in other complementary experiments of 30-cyclic loadings.

To study the response of NiTi SMA to distinct cyclic loading rounds, 10 indentations were performed on the same location. Fig. 2 shows the cyclic loading curves with the setup shown in the inset figure. Each cyclic routine consisted of a loading and an unloading stage at a similar rate of 2×10^2 µNsec^{-1}, followed by a 60-sec holding time at the end of the unloading stage while the tip was in a holding position with no contact with the sample. The next cycle was performed by descending the tip on the same indented spot with the similar three sections of the set up. These indentations were conducted ten times.

During the cycles, the indentation machine coordinated a new origin for Z (the indentation direction as Z = 0) for any fresh test when the tip touched the spot for a subsequent indentation. As a result, every indentation curve started from zero Z for a following cycle. As such, before stabilization, the residual depth of each cycle could be calculated by adding up the obtained residual depth to the remaining residual impression of the previous cycle. After cycle 6, where stabilization occurred, the residual depth did not change and the total residual depth remained unchanged. This fact can be observed in Fig. 2 where the residual depth of each individual cycle stabilizes after cycle 6. Similar to Fig. 1 the residual depths increased while the cyclic loading continued towards the 10th cycle. Contrary to Fig. 1, the maximum nanoindentation depth decreased from the first to the last cycle.
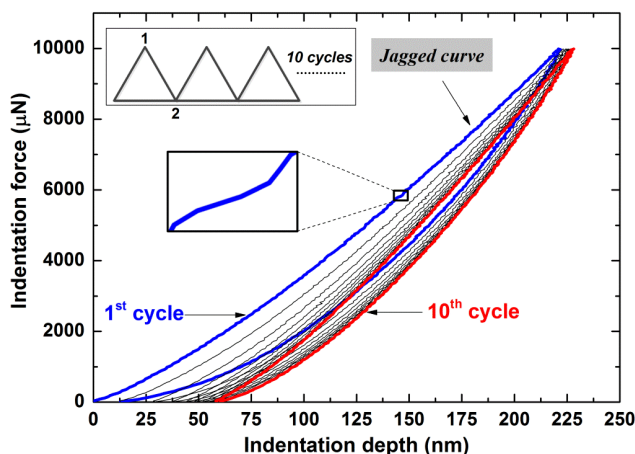
Figure 2 | Indentation curves of 10 consecutive cycles with a 3.61 µm radius tip and 10000 µN maximum indentation force on the same indentation spot. Inset figure: The triangular set up of cyclic loading on NiTi SMA with a 60 sec holding time after each unloading stage.

The hysteresis areas of indentation curves are shown in Fig. 3. The dissipated energy for the data in Fig. 1 (cyclic loading with no holding time) decreased from ~0.23 nanoJoules in the first cycle and approached ~0.1 nanoJoules in the 10th cycle. The increasing trend of the hysteresis areas for data in Fig. 2 (cyclic loading with 60-sec holding time) started from ~0.1 nanoJoules in the first cycle and stabilized at ~0.18 nanoJoules in the 6th to 10th cycles. The hysteresis areas for both cyclic set ups were similar in the 3rd–4th cycles and major stability occurred after 6 indentations. The results also suggest that, in contrast to Fig. 1, the hysteresis area in Fig. 2 did not decline, rather it did significantly increase during the ten cycles.

Thermomechanical behaviour of NiTi SMAs. In a complete round of a loading-unloading stage for NiTi SMA, the hysteresis stress is generally defined in a simple form as[14]:

$$H = \sigma_{AM}(\theta, \dot{\varepsilon}) - \sigma_{MA}(\theta, \dot{\varepsilon}) \tag{1}$$

θ and $\dot{\varepsilon}$, σ_{AM}, σ_{MA} are temperature, rate (either strain or loading), forward phase transformation stress (austenite (A) to martensite (M)) and reverse phase transformation stress (M to A). During the loading stage on an austenitic NiTi SMA, the process of phase transformation generally consists of an elastic deformation of austenite phase, a transformation from the austenite phase to the martensite phase at the phase transformation stress (σ_{AM}), an

Figure 1 | Indentation curve of 10 consecutive cycles with a 3.61 µm radius tip and 10000 µN maximum indentation force. Inset figure: The triangular set up for cyclic loading on the NiTi SMA.

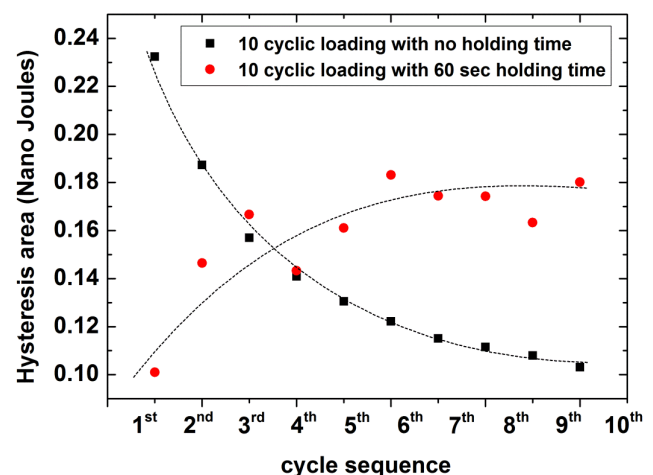**Figure 3 | Hysteresis area of each cycle for two cyclic set ups.**

elastic deformation of martensite phase and the plastic deformation of martensite phase. At the unloading stage, the resultant elastically deformed martensite phase reverses until the stress reaches the reverse phase transition (σ_{MA}). At this stress, the reverse phase transformation continues until all martensitic phase transforms to the austenite phase. The hysteresis stress (H in Eq. 1) represents the net applied stress to perform the phase transformation process from the beginning of the forward phase transition towards the end of the reverse phase transition.

In a simple form, the temperature dependent stresses in Eq. 1 have linear relationships with temperature through Clausius-Claperon equations[31]:

$$\sigma_{AM}(\theta) = \sigma_{AM}(\theta_0) + b_{AM} \cdot (\theta - \theta_0), \; b_{AM} > 1 \tag{2}$$

$$\sigma_{MA}(\theta) = \sigma_{MA}(\theta_0) + b_{MA} \cdot (\theta - \theta_0), \; b_{MA} > 1 \tag{3}$$

θ_0, b_{AM}, b_{MA} are initial temperature and Clausius-Claperon coefficients. Eqs. (2) and (3) reveal the increasing trend of forward and reverse phase transformation stresses of NiTi SMA in the case of a temperature increase. It will be discussed in other sections that a higher rate results in a higher temperature depending on the setup[12,13]. Therefore, the rate has been separated from the temperature in Eq. 1 to highlight the possibility of a similar effect in the absence of one another.

Eq. 1–3 are commonly applied for tensile tests, however, they can be generalized for indentation tests. The corresponding relations between a compression and a tensile test can be obtained when the normal pressure on the projected indentation contact area of phase transformed zone is about three times the uniaxial compressive transition stress[36]. In addition, with an asymmetrical trend of martensite deformation in a uniaxial compression-tension test, the uniaxial compressive transition stress is about 1.5 times the tensile transition stress[37].

Eq. 1 is used to define the dissipated energy of NiTi SMA during a complete round of the forward and reverse phase transition which is defined as[13]:

$$Hys = H \cdot \varepsilon_m \tag{4}$$

where ε_m is the maximum phase transition strain.

The parameters in Eq. 1–4 can be limited to an isothermal loading condition (slow loading rates) with constant σ_{AM} and σ_{MA}. In real applications, the alloy usually experiences a non-isothermal condition in the indented bulk during the loading-unloading stages. This has a significant effect on the parameters in Eq. 1–4 due to the high sensitivity of NiTi SMA to temperature[38]. During a cyclic loading, the variation of temperature is the result of a change in the rate, either loading rate or heating/cooling rate[3]. As such, the variation of hysteresis energy is governed by two main sources: the loading-unloading rate in each cycle and the total accumulated heat during a cyclic set up.

In a nanoindentation test with the dominancy of conduction, the critical time parameter for heat transfer is defined as[26]:

$$t_{critical} = \frac{t_{cd}}{t_L} \tag{5}$$

t_L, t_{cd} are the characteristic loading time and conduction time defined as:

$$t_{cd} = \frac{\alpha' \cdot \lambda \cdot R^2}{k \cdot \varepsilon^2} \tag{6}$$

$$t_L = \frac{\beta \cdot F_{max}}{\dot{F}} \tag{7}$$

α' is the state coefficient (depending on the tip and the initial condition), λ is the heat capacity per unit volume, R is the tip radius, k is the thermal conductivity, ε is the equivalent indentation strain for a spherical tip defined as $\frac{0.2a}{R}$, where a is the indentation contact radius[39], β is the rate coefficient[28], F_{max} is the maximum load and $\dot{F}$ is the loading rate. The amount of heat transfer energy also depends on the contact area with the tip (heat transfer through the tip) and the interface area (heat transfer through the bulk). In a tensile test, the amount of phase transition volume and its resultant heat release are limited to a certain amount for the tested piece's geometry[14]. In contrast, during an indentation test, with an unlimited bulk beneath the tip, the time for releasing latent heat in Eq. (7) is determined by the maximum load and the loading rate (not by ε_m).

The critical and characteristic times in Eq. 5–7 determine the isothermal, rate dependent and adiabatic performance zones for a thermomechanical SMA[26,38,39]. The critical time (Eq. 5), as one of the main parameters in a dynamic loading on thermomechanical materials, introduces a balance limit between the conduction time (heat transfer time) and the loading time (heat release time). In general, for an isothermal condition when $t_{cd} \gg t_L$, the temperature remains unchanged equal to the initial loading temperature. Preventing the temperature increase by conducting most of the released latent heat concludes in an unchanged phase transition stress. This results in a higher amount of phase transformed volume. A longer cooling time (route 1-2-3 in the inset Fig. 2) and a higher thermal relaxation in an isothermal condition stabilize the temperature in the transformed zone as well as in the non-transformed zone which is subsequently transformed during the loading process. The stabilized temperature has been reported to be equal to the initial temperature in an isothermal macroscale tensile condition with a convection dominancy[31]. In the rate-dependent or adiabatic condition, when $t_{cd} \ll t_L$, the temperature builds up. This phenomenon is due to either faster loadings (high amount of heat release and less conducted heat) or non-isothermal consecutive cyclic loadings (accumulated untransformed/unabsorbed heat). This leads to an increase in the temperature and the phase transition stress and, therefore, less phase transformed volume and dissipated energy. In the next section, as technologies to trace the phase transition and to measure the temperature of the nanoscale bulk during an indentation test are not yet available[38], we performed a numerical simulation at different temperatures to support the above rationale.

Numerical simulation-constitutive theory. A phenomenological 3D constitutive model was implemented into ABAQUS 2010. The model is based on the general inelastic frame and the total strain tensor $\boldsymbol{\varepsilon}$ is disassembled into elastic strain $\boldsymbol{\varepsilon}^e$, the transformation strain $\boldsymbol{\varepsilon}^{tr}$, and martensite plastic strain $\boldsymbol{\varepsilon}^p$:

$$\boldsymbol{\varepsilon} = \boldsymbol{\varepsilon}^e + \boldsymbol{\varepsilon}^{tr} + \boldsymbol{\varepsilon}^p \tag{8}$$

The elastic strain is assumed to be related to the stress by the effective elastic modulus tensor $\mathbf{D}_{am}(z)$:

$$\boldsymbol{\sigma} = \mathbf{D}_{am}(z) : \boldsymbol{\varepsilon}^e = \mathbf{D}_{am}(z){:}(\boldsymbol{\varepsilon} - \boldsymbol{\varepsilon}^{tr} - \boldsymbol{\varepsilon}^p) \tag{9}$$

where $\boldsymbol{\sigma}$ is the stress and z is the martensite volume fraction. The model is constructed from the assumption that the martensitic transformation mechanism is associated with an active reorientation process, described by the following equation:

$$\boldsymbol{\varepsilon}^{tr} = \varepsilon_m z \frac{\partial F(\boldsymbol{\sigma}, \theta)}{\partial \boldsymbol{\sigma}} \tag{10}$$

$F(\boldsymbol{\sigma}, \theta)$ is the loading function that drives the martensitic transformation. In this simulation, the Drucker-Prager type of loading function is used for the forward and reverse transformation:

$$F(\boldsymbol{\sigma}, \theta) = \|\mathbf{s}\| + 3\alpha P - b_{AM}\theta \tag{11}$$
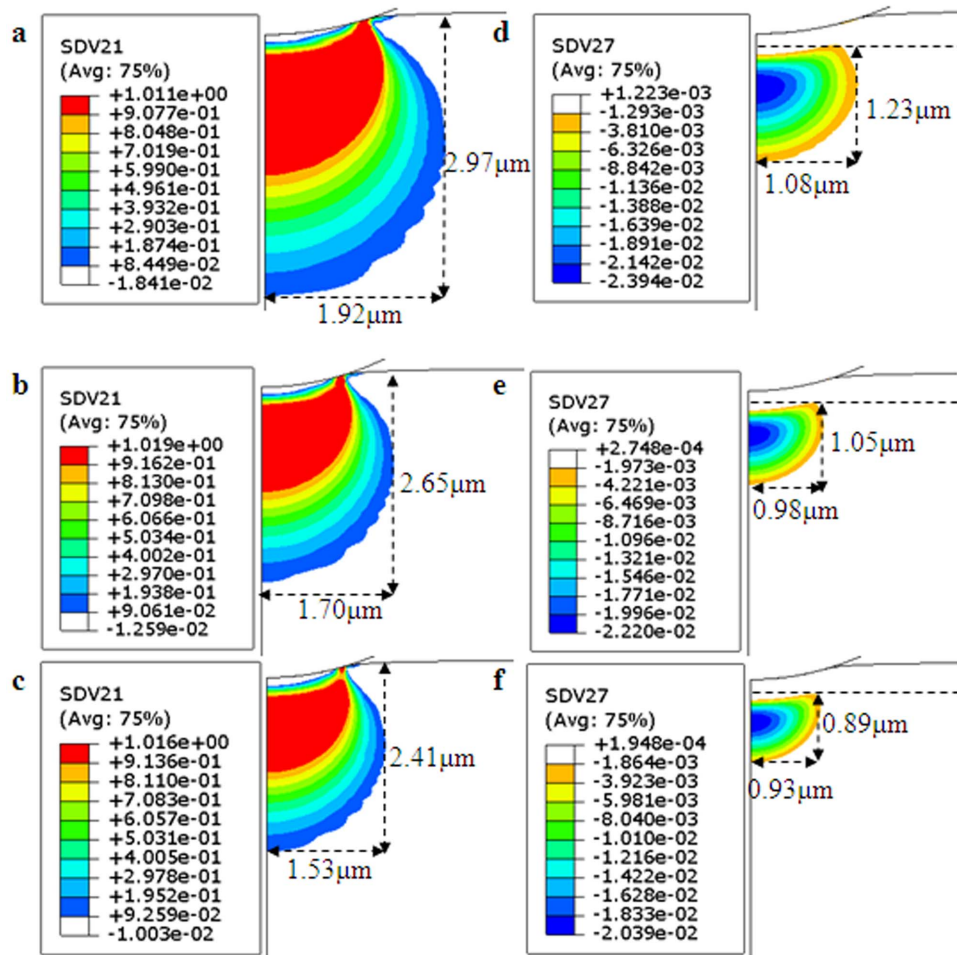
Figure 4 | Finite element simulation results for indentations using a 3.61 μm radius tip: The volume fraction of martensite phase at (a) 20˚C (b) 35˚C (c) 50˚C, and the plastic strain at (d) 20˚C, (e) 35˚C, (f) 50˚C.

$$F(\boldsymbol{\sigma},\theta) = \|\mathbf{s}\| + 3\alpha P - b_{MA}\theta \qquad (12)$$

$\mathbf{s} = \boldsymbol{\sigma} - P\mathbf{I}$ is the deviatoric stress tensor where $P = \frac{1}{3}\boldsymbol{\sigma}{:}\mathbf{I}$ is the hydrostatic pressure, $\mathbf{I}$ is the second rank unit tensor, and α reflects the anisotropic transformation responses in tension and compression processes.

After finishing the forward transformation, the plastic deformation occurs in the stress-induced martensite if the applying stress reaches the plastic yield stress of the martensite phase. Assuming that the plastic deformation obeys the von Mises yielding condition, the plastic strain can be shown as:

$$\boldsymbol{\varepsilon}^p = \lambda'\frac{\partial F_y}{\partial \boldsymbol{\sigma}} = \sqrt{\frac{3}{2}}\, p\,\frac{\mathbf{s}}{\|\mathbf{s}\|} \qquad (13)$$

where p is the effective plastic strain, λ' is the plastic multiplier, and F_y is the martensite plastic yield function.

The material properties are selected as: same elasticity modulus of phases: $E_A = E_M = 31\ GPa$, same Poisson's ratio of phases: $\nu_A = \nu_M = 0.33$, $b_{AM} = 6.0\ MPa/K$, $b_{MA} = 7.6\ MPa/K$, maximum phase transition strain: $\varepsilon_m = 0.048$, yield stress of the martensite phase: $\sigma_y^M = 900\ GPa$, testing temperatures: 20˚C, 35˚C, 50˚C, $\alpha = 0.178$, $\sigma_{AM}^s = 385\ MPa$, $\sigma_{AM}^f = 402\ MPa$, $\sigma_{MA}^s = 215\ MPa$, $\sigma_{MA}^f = 198\ MPa$, where superscript s and f show the start and finishing stress of the forward transformation (AM) or the reverse transformation (MA).

In this finite element simulation, the spherical indentation was modeled as a 2D axisymmetric problem. Roller boundary condition is imposed on the symmetric axis of the sample and the bottom is constrained in both radial and axial directions. The minimum element length in the contact zone is 12.5 nm. To avoid the influence of boundary condition, the side length of the sample is thirty times larger than the radius of the indenter. A preliminary mesh sensitivity analysis was performed to ensure that the simulated results were insensitive to the element size in the contact zone. The results of the above simulation are presented in Fig. 4 (a–f). These figures show that the transformation volume and the martensitic plastic zone decrease with an increase in the testing temperature.

Discussion

The hysteresis energy variation in Fig. 3 can be explained by Eqs. 1–3. By raising the temperature both σ_{AM} (θ) and σ_{MA} (θ) increase. During this stage, experimental reports show that at higher rates the growth of σ_{MA} (θ) is higher than the growth of σ_{AM} (θ) due to the relationship $0 < b_{AM} < b_{MA}$[12,40]. Thus, comparing two isothermal and non-isothermal setups, either at a higher loading-unloading rate or as a result of consecutive cycles, H and Hys (Eq. 4) decrease due to the higher temperature caused by the accumulative heat and a lower cooling time[5]. In fact, the transfer time for 2000 $\mu N/s$ is 10 times lower than the isothermal rate 200 $\mu N/s$. This leads to less heat transfer after each cycle and, therefore, more total heat accumulation after several cycles. While the cycle sequence increases, the phase transition stress also increases due to the increase in temperature

4

(Eq. 2). By increasing the phase transition stress and temperature, the phase transformed volume decreases consequently (see Figs. 4 (a–c)). This phenomenon provides a balance between the phase transition volume and the accumulation heat which results in a constant hysteresis energy. In other words, there is a balance between the conduction time and the released time that concludes in an unaltered trend of hysteresis energy after several cycles.

According to Figs. 4 (d–f), when the temperature increases the plastic deformation also reduces. This fact can be seen in Fig. 1 where during the cyclic loadings the residual depth of each cycle decreases. Fig. 4 also shows that the volume of the bulk with 100% martensite phase (red color zone) is much larger than the volume of the bulk with high plastic deformations, e.g., > 2%. This fact confirms that the main determining characters for SMA's behavior during the cyclic spherical nanoindentation are phase transition and latent heat and not plasticity[25]. As such, the dislocation evolution has relatively similar influence in both setups.

At the isothermal low rate, the hysteresis energy captures the stabilized amount after an increasing trend. With the absence of temperature increase, the hysteresis increase is explained by the reorientation phenomenon in favour of the phase transition in subsequent cycles[20,27]. For the isothermal loading rate, the phase transition stress is lower (more achievable by a similar applied load, 10000 μN) than the transition stress level for the non-isothermal loading rate. Therefore, after stabilization the final hysteresis energy for the rate 200 $\mu N/s$ is expected to be higher than the hysteresis energy for the rate 2000 $\mu N/s$. In brief, with a similar initial condition, the atomic and microstructure degradations influence the cyclic-loading results for the isothermal condition (Fig. 2) and the two time scales govern the hysteresis trend for the higher rate setup (Fig. 1).
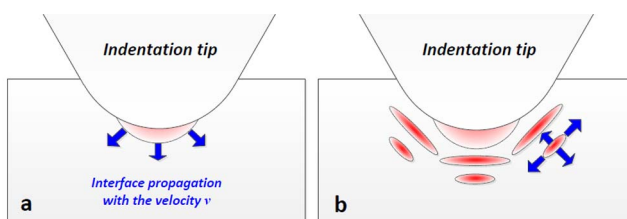
In comparison to the lower rate data, Fig. 3 shows a higher amount of hysteresis energy in the first few cycles for the higher rate setup. There are three possible reasons for this. First, with an increase in the loading rate, stress-induced phase transformed nucleation occurs in an increasing number of different locations (Figs. 5 a, b).

Secondly, the phase transformed volume is propagated by an interface with the velocity of v[31]:

$$v = \frac{r_{ph}}{t_L} \qquad (14)$$

r_{ph} represents the maximum radius of the bulk underneath the tip where the stress is higher than the nucleation phase transition stress. Eq. (14) implies that for a similar size of the loaded bulk, faster load (lower t_L) has a higher velocity of interface propagation. This concludes in a higher phase transformed volume with the resultant larger hysteresis area at higher loading rates for the first few cycles in which the heat has not been significantly accumulated by the following cycles. While the heat is accumulated, the velocity decreases subsequently.

Fig. 5 schematically provides a hypothesis for the nucleation and propagation of the phase transition volume in a nanoindentation process. When the loading rate is in an isothermal condition, the nucleation and propagation of the phase transition volume mostly occur with one or two interfaces at a low speed (Fig. 5a)[31]. As the loading rate increases, the number of nucleation sites and the interface velocity increase (Fig. 5b). The domain spacing between the phase transition sites and the number of nucleation sites have been shown to be proportional to $\dot{\varepsilon}^{-1}$ and $\dot{\varepsilon}$ in the dominancy of the convection (tensile testing)[31]. Similar nucleation and propagation sites in Fig. 5b were recently shown as local micro-plastic hardening and twinning by a MD simulation for indentation experiments[30]. In the present study, compared to the smooth indentation curves for the isothermal rate setup (Fig. 2), the jagged shape of the indentation curves (Fig. 1) for the non-isothermal rate setup is due to numerous new nucleation sites beneath the tip while the load is applying. These sites relax the stress and increase the strain at the time of nucleation.
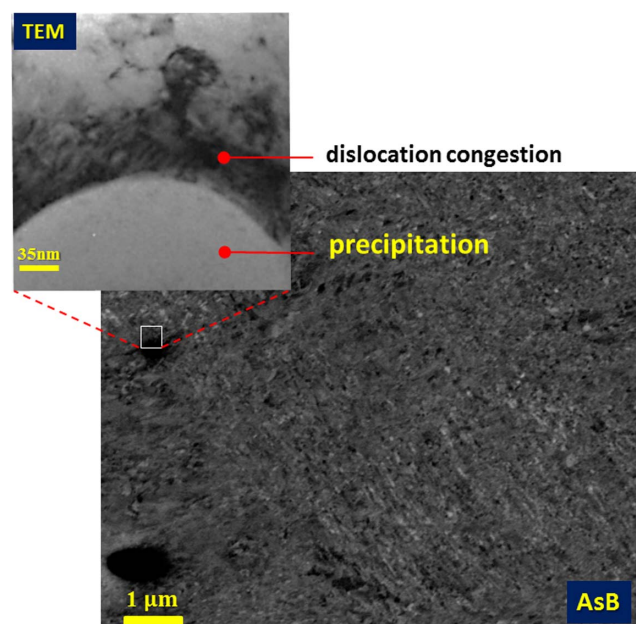
It should be noted that the number of nucleation sites also depends on the defect zones such as inclusions, existent dislocations and precipitations where the stress concentration nucleates the phase transformation. The latter two are shown in Fig. 6 using AsB and TEM. This figure indicates two major single crystal precipitations located at different places of the texture. The dislocation congestion around the precipitations with a hard phase is clearly seen in the TEM image in inset Fig. 6. The existence of these structures in the stressed bulk can be one of the rationale of having either irregular or dissimilar jagged events (nucleated phase transition volume) throughout an indentation curve in Fig. 1.

Furthermore, the activation volume in a thermally activated mechanism has the following relationship[28]:

$$V^* = \sqrt{3}k\theta\left(\frac{\partial \ln \dot{\varepsilon}}{\partial \sigma}\right) = \frac{\sqrt{3}k\theta}{m\sigma} \qquad (15)$$

where $\dot{\varepsilon}$, m and k are strain rate, rate sensitivity and Boltzman's constant. In this equation, the phase transition stress is assigned as σ for NiTi SMA for the applied stress using a spherical tip. By Eq. 15 the previous rationale, higher hysteresis energy in the first few cycles, is validated as the activation volume is larger at higher rates. This can be associated with the higher initial propagation velocity of interface and the larger radius of stressed bulk (Eq. 14).

Thirdly, using Eq. 2 and 3, on increasing the temperature, Eq. 15 degenerates into the following equation:

Figure 5 | Nucleation sites of the phase transition volume and their propagation under the cyclic indentation loading with a lower rate (a), and with a higher rate (b).

Figure 6 | TEM and AsB images of precipitations and the presence of dislocations around them.

5

$$\Delta V^* = \frac{\sqrt{3}k}{mb} \qquad (16)$$

ΔV^* represents either the activation volume variation after each consecutive cycle or the total change in the activation volume after 10 cycles. Eq. 16 shows that unlike ordinary materials with no phase transition, if the temperature increases during the cyclic loading, the activation volume decreases with the ratio $\frac{1}{b}$ (<1) where b is the Clausius-Claperon coefficient shown in Eqs. 2 and 3. This is an additional rationale for a decreasing hysteresis during the cyclic loading with a higher rate (Fig. 3). During the cyclic loading with an isothermal rate, i.e., 200 µN/s, the activation volume remains unchanged due to the constant temperature.

It is not coincidental that accumulated heat during the cyclic loading has a close correlation with the initial condition, e.g., initial temperature and hysteresis energy. In cyclic tensile loadings, the stable mean temperature and its fluctuation depend on the initial temperature, its initial hysteresis energy and the characteristic time scale of convection and the loading-unloading time. The total transferred heat to the ambient remain unchanged after several cycles. Similarly, in nanoindentation, the final condition of each cycle, which is the initial condition for the subsequent cycle, plays an important role in raising the accumulated heat at the end of 10 cycles.

In summary, the behavior of NiTi SMA was studied under two different cyclic loading setups and a hypothesis was provided on the nucleation of the phase transformation volume in a nanoscale stressed bulk. To obtain an improved cooling process, a cyclic loading with a lower rate and a holding time was applied on NiTi SMA. In this setup, the hysteresis energy increases from the initial cycles to a stabilized magnitude in subsequent cycles. This trend is explained by the reorientation that situates the alloy in a favourable modal energy for the subsequent cycles. In the second cyclic loading setup with a higher rate and a weaker cooling process, the time balance between the heat release and the heat conduction determines the trend of lowering the hysteresis energy in subsequent cycles.

Methods

Using a differential scanning calorimeter (DSC, TA-Q1000), the austenite finish temperature (A_f) of NiTi SMA was measured as 19°C. The material was initially in the austenite phase and the martensite phase was induced by the applied compressive stress with a superelastic behavior. The nominal alloy composition as determined by a high resolution X-ray diffraction spectroscopy (XRD, PW1825) was 56.4% Ni and 43.6% Ti by weight. The grain size was in the range of 50–100 nm as observed by a transmission electron microscopy (TEM, 200 kV: JEM-2100F). Angle selective Backscattered electron (AsB) images of orientation and precipitation were obtained using a Zeiss Supra 55VP. The sheet was cut into pieces (5 mm × 5 mm) and polished using a series of silicon carbide and diamond papers until the average surface roughness was less than 6 nm measured using a 3D surface profiler (SPM, NT3300). In order to achieve a well-controlled compression process, an in situ nanoindentation machine, a Hysitron nanoindentor (TI 900 Triboindenter) was used. Before carrying out tests, the instrument was carefully calibrated using standard procedures. The nanoindentation tests were conducted at room temperature (23°C) in a quasi-static mode using a spherical diamond tip with a 3.61 µm radius. A constant maximum load of 10000 µN was applied in all tests. The indentation load was controlled by an ultrafine piezoelectric beam in the machine.

1. Amini, A., Yan, W. & Sun, Q. P. Depth dependency of indentation hardness during solid-state phase transition of shape memory alloys. *Appl. Phys. Lett.* **99**, 021901 (2011).
2. Amini, A. & Cheng, C. Nature of hardness evolution in nanocrystalline NiTi shape memory alloys during solid-state phase transition. *Sci. Rep.* **3**, 2476 (2013).
3. Amini, A., Cheng, C. & Asgari, A. Combinational rate effects on the performance of nano-grained pseudoelastic Nitinols. *Mater. Lett.* **105**, 98–101 (2013).
4. Frick, C. P., Lang, T. W., Spark, K. & Gall, K. Stress-induced martensitic transformations and shape memory at nanometer scales. *Acta Mater.* **54**, 2223–2234 (2006).
5. Predki, W., Klonne, M. & Knopik, A. Cyclic torsional loading of pseudoelastic NiTi shape memory alloys: Damping and fatigue failure. *Mater. Sci. Eng. A.* **417**, 182–189 (2006).
6. Gloanec, A. L., Bilotta, G. & Gerland, M. Deformation mechanisms in a TiNi shape memory alloy during cyclic loading. *Mater. Sci. Eng. A.* **564**, 351–358 (2012).
7. Gloanec, A. L., Cerracchio, P., Reynier, B., Van Herpen, A. & Riberty, P. Fatigue crack initiation and propagation of a TiNi shape memory alloy. *Scripta Mater.* **62**, 786–789 (2010).
8. Fei, X., Zhang, Y., Grummon, D. S. & Cheng, Y. T. Indentation-induced two-way shape memory surfaces. *J. Mater. Res.* **24**, 823–830 (2009).
9. Fei, X., Grummon, D. S., Ye, C., Cheng, G. J. & Cheng, Y. T. Surface form memory in NiTi shape memory alloys by laser shock indentation. *J. Mater. Sci.* 1–7 (2012).
10. Arciniegas, M., Gaillard, Y., Pena, J., Manero, J. & Gil, F. Thermoelastic phase transformation in TiNi alloys under cyclic instrumented indentation. *Intermet.* **17**, 784–791 (2009).
11. Matsumoto, H., Kondo, K. I., Dohi, S. & Sawaoka, A. Shock compaction of NiTi alloy powder. *J. Mater. Sci.* **22**, 581–586 (1987).
12. Paradis, A., Terriault, P., Brailovski, V. & Torra, V. On the partial recovery of residual strain accumulated during an interrupted cyclic loading of NiTi shape memory alloys. *Smart Mater. Struct.* **17**, 065027 (2008).
13. He, Y. & Sun, Q. P. Frequency-dependent temperature evolution in NiTi shape memory alloy under cyclic loading. *Smart Mater. Struct.* **19**, 115014 (2010).
14. He, Y. & Sun, Q. P. On non-monotonic rate dependence of stress hysteresis of superelastic shape memory alloy bars. *Int. J. Solids. Struct.* **48**, 1688–1695 (2011).
15. Igata, N., Urahashi, N., Sasaki, M. & Kogo, Y. High damping capacity due to two-step phase transformation in Ni–Ti, Ni–Ti–Cu, and Fe–Cr–Mn alloys. *J. Alloys Compd.* **355**, 85–89 (2003).
16. Chapman, C., Eshghinejad, A. & Elahinia, M. Torsional behavior of NiTi wires and tubes: modeling and experimentation. *J. Intel. Mater. Sys. Struct.* **22**, 1239–1248 (2011).
17. Gédouin, P.-A., Chirani, S. A. & Calloch, S. Phase proportioning in CuAlBe shape memory alloys during thermomechanical loadings using electric resistance variation. *Int. J. Plasticity* **26**, 258–272 (2010).
18. Delville, R., Malard, B., Pilch, J., Sittner, P. & Schryvers, D. Transmission electron microscopy investigation of dislocation slip during superelastic cycling of Ni–Ti wires. *Int. J. Plasticity* **27**, 282–297 (2011).
19. Arghavani, J., Auricchio, F., Naghdabadi, R., Reali, A. & Sohrabpour, S. A 3-D phenomenological constitutive model for shape memory alloys under multiaxial loadings. *Int. J. Plasticity* **26**, 976–991 (2010).
20. Ma, X. G. & Komvopoulos, K. Pseudoelasticity of shape-memory titanium–nickel films subjected to dynamic nanoindentation. *Appl. Phys. Lett.* **84**, 4274–4276 (2004).
21. Fei, X., O'Connell, C. J., Grummon, D. & Cheng, Y. T. Surface form memory by indentation and planarization of NiTi: displacements and mechanical energy density during constrained recovery. *J. Mater. Sci.* **46**, 7401–7409 (2011).
22. Millett, J., Bourne, N. & Gray, G. Behavior of the shape memory alloy NiTi during one-dimensional shock loading. *J. Appl. Phys.* **92**, 3107–3110 (2002).
23. Yan, W., Sun, Q. P. & Liu, H. Y. Spherical indentation hardness of shape memory alloys. *Mater. Sci. Eng. A.* **425**, 278–285 (2006).
24. Kang, G. & Yan, W. Effects of phase transition on the hardness of shape memory alloys. *Appl. Phys. Lett.* **94**, 261906 (2009).
25. Yan, W., Amini, A. & Sun, Q. P. On anomalous depth-dependency of the hardness of NiTi shape memory alloys in spherical nanoindentation. *J. Mater. Res.* **28**, 2031–2039 (2013).
26. Amini, A., He, Y. & Sun, Q. P. Loading rate dependency of maximum nanoindentation depth in nano-grained NiTi shape memory alloy. *Mater. Lett.* **65**, 464–466 (2011).
27. Zhang, H. S. & Komvopoulos, K. Nanoscale pseudoelasticity of single-crystal Cu–Al–Ni shape-memory alloy induced by cyclic nanoindentation. *J. Mater. Sci.* **41**, 5021–5024 (2006).
28. Somekawa, H. & Schuh, C. A. Effect of solid solution elements on nanoindentation hardness, rate dependence, and incipient plasticity in fine grained magnesium alloys. *Acta Mater.* **59**, 7554–7563 (2011).
29. Somekawa, H. & Schuh, C. A. Nanoindentation behavior and deformed microstructures in coarse-grained magnesium alloys. *Scripta Mater.* **68**, 416–419 (2012).
30. Deng, C. & Schuh, C. A. Atomistic mechanisms of cyclic hardening in metallic glass. *Appl. Phys. Lett.* **100**, 251909 (2012).
31. Zhang, X., Feng, P., He, Y., Yu, T. & Sun, Q. P. Experimental study on rate dependence of macroscopic domain and stress hysteresis in NiTi shape memory alloy strips. *Int. J. Mech. Sci.* **52**, 1660–1670 (2010).
32. He, Y. & Sun, Q. P. Rate-dependent domain spacing in a stretched NiTi strip. *Int. J. Solids Struct.* **47**, 2775–2783 (2010).
33. Zhang, Y., Cheng, Y.-T. & Grummom, D. S. Novel tribological systems using shape memory alloys and thin films. *Surf. Coat. Tech.* **202**, 998–1002 (2007).
34. Amini, A. et al. Effect of graphene on thermomechanical behavior of NiTi shape memory alloy during nano-scale phase transition. *Scripta Mater.* **68**, 420–423 (2012).
35. Cheng, C. et al. Heat transfer across the interface between nanoscale solids and gas. *ACS nano* **5**, 10102–10107 (2011).
36. Qiana, L., Xiao, X., Sun, Q. P. & Yu, T. Anomalous relationship between hardness and wear properties of a superelastic nickel–titanium alloy. *Appl. Phys. Lett.* **84**, 1076 (2004).

37. Orgéas, L. & Favier, D. Stress-induced martensitic transformation of a NiTi alloy in isothermal shear, tension and compression. *Acta Mater.* **46**, 5579–5591 (1998).
38. Amini, A. *et al.* Temperature variations at nano-scale level in phase transformed nanocrystalline NiTi shape memory alloys adjacent to graphene layers. *Nanoscale* **5**, 6479–6484 (2013).
39. Amini, A., Beladi, H., Hameed, N. & Will, F. Effects of dynamic loading on nano-scale depth-recovery and damping property of single crystal CuAlNi shape memory alloy. *J. Alloys Compd.* **545**, 222–224 (2012).
40. Morin, C., Moumni, Z. & Zaki, W. A constitutive model for shape memory alloys accounting for thermomechanical coupling. *Int. J. Plasticity* **27**, 748–767 (2011).

Author contributions

A.A. designed the research, wrote the paper, performed the nanoindentation and material characterizations and analysed the indentation results, C.C. performed the TEM experiments and incorporated in experimental analyses, Q.K. performed the numerical simulations, M.N. conducted the AsB experiments and their analysis, and H.S. incorporated in the interpretation of experimental results.

Additional information

Competing financial interests: The authors declare no competing financial interests.

How to cite this article: Amini, A., Cheng, C., Kan, Q.H., Naebe, M. & Song, H.S. Phase Transformation Evolution in NiTi Shape Memory Alloy under Cyclic Nanoindentation Loadings at Dissimilar Rates. *Sci. Rep.* **3**, 3412; DOI:10.1038/srep03412 (2013).